CILAMCE 2017

Florianópolis - Santa Catarina - Brazil

MODELING SIMULATION OF FLOW OVER A ROTATING CIRCULAR CYLINDER WITH VORTEX-INDUCED VIBRATION

Túlio Alves Rodrigues

Elie Luis Martinez Padilla

tulio.rodrigues@ufu.br

epadilla@ufu.br

Federal University of Uberlândia

Av. João Naves de Ávila, 38408-100, Minas Gerais, Brazil

Jonatas Emmanuel Borges

jonatasborges@cpd.ufmt.br

Federal University of Mato Grosso

Av. Fernando Corrêa da Costa, 78060-900, Cuiabá, Mato Grosso, Brazil

Abstract. *The present work presents the analysis of incompressible flows around a circular cylinder with rotation for two degrees of freedom, whose Reynolds value was set at 150, varying at reduced speed. The validation of the results is also presented through comparison with literature data. A methodology was used combining the finite volume method and the immersed boundary method, the latter being used to represent the cylinder. In the time discretization,the fourth-order Runge-Kutta method was used, as well as the fractional step method for the pressure-velocity coupling. The results, based on the solution of the Navier-Stokes equations, include fields of vorticity, history of the position and mean position of the cylinder, variation of displacement amplitude with reduced velocity, variation of drag and lift coefficients and also the trajectory of the Cylinder with reduced velocity. By the results, it was possible to analyze the interference of the reduced velocity in the formation of structures, in other words, in the types of structures formed and at the moment in which they begin to modify the amplitude, influencing in the phenomenon of synchronization.*

Keywords: *Fluid mechanics, Fluid structure interaction, Immersed boundary method, Finite volume method*

1 INTRODUCTION

Studies around solid bodies have been the subject of numerous theoretical, numerical and experimental studies due to the high frequency that these can be found in nature and in technological applications. When a flow comes in contact with a structure, it is subjected to a fluid-dynamic pressure, which can generate deformation or movement in the structure. As these effects occur, the fields of pressure and velocity of the flow are changed, thus changing the forces that affect the structure. This type of interaction is called fluid structure interaction (FSI) (Nascimento, 2016).

Within this type of interaction, we have the vortex-induced vibration (VIV) phenomenon of a structure, which consists of the interaction of structures with external flows. The study of the release of vortices of a cylinder, has been object of several engineering studies, due to its great importance. Some of the main configurations are: fixed cylinders, cylinders anchored by spring-damper systems (with one or two degrees of freedom), fixed cylinders with rotation, which are little discussed in the literature and cylinders with rotation with vibration. The rotation rate (α) has great importance in the formed structures due to the flow. Understanding as well as the same influence the flow around the cylinder, we can alter the structures formed and even inhibit the formation of them, as will be approached in this study.

In this context, this study presents the modeling and two-dimensional simulation of flows on a cylindrical body, for Reynolds of 150 and $\alpha = 0;\ 0.5$ and 1.0, using the immersed boundary method for modeling the immersed geometry coupled to the finite volume method.

2 PHYSICAL MODEL

The present work consists of the modeling and simulation of an incompressible two-dimensional flow on a rotating circular cylinder, anchored with spring-damping system that allows the structure two degrees of freedom, as shown in Fig. 1, below.

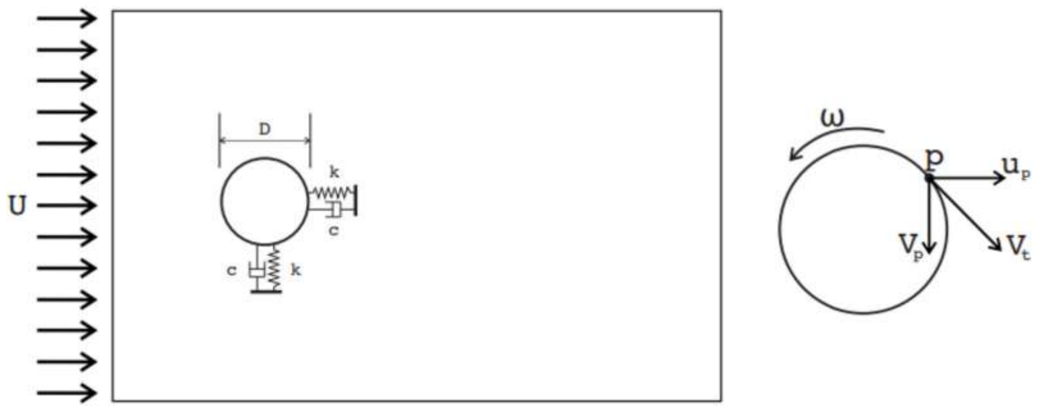

Figure 1: Physical model with two degrees of freedom.

The cylinder has a diameter of D, the springs have the same rigidity equal to k, shock absorbers with equal damping constants c and angular velocity ω $[rad/s]$, obtained by means of the rotation rate α, defined by:

$$\alpha = \frac{\omega D}{2U}, \tag{1}$$

where U is the velocity imposed by the flow. As shown in Fig. 1, we have the tangential velocity V_t parsed at any point p, with its components u_p and v_p projected in their respective directions.

3 MATHEMATICAL MODELS

3.1 Immersed boundary method - IBM

The immersed boundary methodology proposes to use a regular Eulerian mesh for the whole domain and to represent the immersed body a second mesh, Lagrangean, was used. As seen in Fig. 2, both are independent, facilitating the representation of complex and even mobile and deformable geometries.

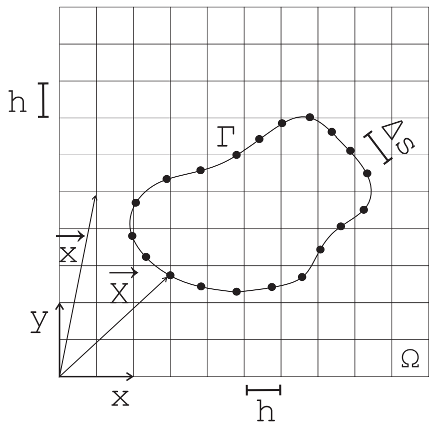

Figure 2: Sketch of domains used in the Immersed Boundary methodology.

3.2 Fluid modeling - Eulerian domain

For the fluid modeling, the Navier-Stokes equations Eq. 2 and the mass conservation equation Eq. 3 valid for the domain (Ω) of Fig. 2. The hypotheses considered are: Newtonian fluid, incompressible flows, physical properties of the fluid constant and without thermal transfer.

$$\frac{\partial u_i}{\partial t} + \frac{\partial u_i u_j}{\partial x_j} = -\frac{1}{\rho}\frac{\partial p}{\partial x_i} + \nu \frac{\partial^2 u_i}{\partial x_j \partial x_j} + f_i, \tag{2}$$

$$\frac{\partial u_j}{\partial x_j} = 0, \tag{3}$$

where $p = p^*/\rho + gz$; p^* is the static pressure in $[N/m^2]$; z is the vertical dimension aligned as gravity vector $\overrightarrow{g}$ in the vertical direction and positive upwards; ρ $[kg/m^3]$ e ν $[m^2/s]$ are the specific mass and kinematic viscosity, respectively; u_i $[m/s]$ is the ith component of velocity; p $[N/m^2]$ is the pressure and $f_i = f_i^*/\rho$ is the ith term source of force, where f_i^* $[N/m^3]$.

3.3 Coupling the Eulerian and Lagrangean domains

The term f_i that appears in Eq. 2, can be considered as a mathematical representation of field forces. In IBM, this term represents the immersed interface of the Eulerian domain (Ω).

In the present study, was used the hat function W_h Eq. 4, which is equivalent to a bilinear interpolation (Su et al., 2007).

$$W_h(r) = \begin{cases} 1 - |r| & se \quad 0 \leq |r| \leq 1 \\ 0 & se \quad 1 < |r| \end{cases}, \tag{4}$$

3.4 Lagrangean force

Within the immersed boundary methodology, it is necessary to describe the lagrangean force calculation model $\overrightarrow{F}(\overrightarrow{x_k}, t)$. The present work uses the Direct Force (DF) imposition method.

Isolating the term f_i from Eq. 2, the Eulerian force field is obtained. As we are working with the continuum hypothesis and the Lagrangian domain is continuous in the Eulerian, we have the lagrangeado force field:

$$F_i(\overrightarrow{X}, t) = \frac{\partial U_i}{\partial t} + \underbrace{\frac{1}{\rho}\frac{\partial P}{\partial x_i} + \left[\frac{\partial (U_i U_j)}{\partial x_j}\right] - \nu \frac{\partial^2 U_i}{\partial x_j \partial x_j}}_{\text{RHS}} \tag{5}$$

where the uppercase variables are related to the Lagrangian domain. The Eq. (5) represents Newton's second law applied to the fluid particles that are located at the fluid-fluid and fluid-solid interface.

After mathematical manipulations, we obtain the Eulerian force field:

$$u_i^{t+\Delta t} = u_i^* + \Delta t f_i, \tag{6}$$

where u_i^* is the corrected velocity field.

3.5 Multi-Direct Forcing - MDF

Wang et al., (2008) have proposed a process whose objective is to ensure that the velocity of the fluid on the immersed interface is equal to the speed of the boundary, as it should theoretically be called Multi-Direct Forcing (MDF), in order to improve the accuracy of the method.

Before advancing to the next time step, the velocity field u_i^{it}, is again interpolated, obtaining a new force field which is still closer to the non-slip condition.

3.6 Structural Modeling

To model the problem, the basic kinematics equations that relate position, velocity and acceleration, as presented in Nascimento (2016), were used.

From the free-body diagram and based on an inertial axis as a reference, we have the model of the motion of the structure, Eq. 7:

$$-\overrightarrow{F}_{spring} - \overrightarrow{F}_{damper} + \overrightarrow{F}_{fluid} = m_s \frac{d^2 r_{OO'i}}{dt^2}, \tag{7}$$

where $\overrightarrow{F}_{spring}$ represents the elastic force, $\overrightarrow{F}_{damper}$ is the force arising from the damper, $\overrightarrow{F}_{fluid}$ represents drag force, $\frac{d^2 r_{OO'i}}{dt^2}$ acceleration and m_s is the mass of the structure.

After some manipulation, as can be seen in Nascimento (2016), we obtain the following equation:

$$m_s \frac{d^2 r_{OO'i}}{dt^2} + c\frac{r_{OO'i}}{dt} + k r_{OO'i} = \frac{Fc_i \Delta s \Delta x \rho_f}{\Delta t}, \tag{8}$$

where Fc_i is the fluid dynamic force obtained by the MDF and Δs e Δx are the lengths required to calculate the volume of fluid related to each lagrangean point.

As suggested by Chern et al., (2014), the Eq. 8 has to be dimensionless. Using the terms shown in Tab. 1 below, obtain the Eq. 9.

Table 1: Groups of dimensionless ones according to two-dimensional model in the plane xy (Chern et al., 2014), where L is the unit length in the z direction.

Description	parameter	dimensionlessness
time	t^*	$\frac{tu_\infty}{D}$
mass ratio	m^*	$\frac{4m}{\pi D^2 \rho L}$
damping ratio	ζ	$\frac{c}{2\sqrt{km_s}}$
reduced speed	U_r^*	$\frac{u_\infty}{f_n D}$
reduced natural frequency	f_n^*	$\frac{f_n D}{u_\infty}$
displacement	$r^*_{AB_i}$	$\frac{r_{AB_i}}{D}$

$$\left(\frac{d^2 r_{OO'i}}{dt^2}\right) + \frac{4\pi\zeta}{U_r^*}\left(\frac{dr_{OO'i}}{dt}\right) + \left(\frac{2\pi}{U_r^*}\right) r^*_{OO'i} = \frac{2Coef}{\pi m^*}. \tag{9}$$

where $Coef$ represents the lift coefficient C_l or the drag coefficient C_d, varying according to the direction in which the flow is analyzed.

In order to solve the equations of the structure, fourth order runge kutta was used, as can be observed in the work of Su et al. (2007).

4 NUMERICAL MODELS

The numerical discretization based on the finite volume method FVM uses the integration of the partial differential equations (EDP) in each volume of elementary control. Integrating the momentum equation Eq. 2, on the elementary volume, in a displaced mesh and in a given time and space, we have:

$$\int_t^{t+\Delta t}\int_{\forall}\frac{\partial u}{\partial t}dtd\forall = -\int_t^{t+\Delta t}\int_{\forall}\frac{\partial (uu)}{\partial x}dtd\forall - \int_t^{t+\Delta t}\int_{\forall}\frac{\partial (uv)}{\partial y}dtd\forall + \\ + \int_t^{t+\Delta t}\int_{\forall}\frac{1}{\rho}\frac{\partial P}{\partial x}dtd\forall + \int_t^{t+\Delta t}\int_{\forall}\nu\left(\frac{\partial^2 u}{\partial x^2}+\frac{\partial^2 u}{\partial y^2}\right)dtd\forall, \tag{10}$$

$$\int_t^{t+\Delta t}\int_{\forall}\frac{\partial v}{\partial t}dtd\forall = -\int_t^{t+\Delta t}\int_{\forall}\frac{\partial (uv)}{\partial x}dtd\forall - \int_t^{t+\Delta t}\int_{\forall}\frac{\partial (vv)}{\partial y}dtd\forall + \\ + \int_t^{t+\Delta t}\int_{\forall}\frac{1}{\rho}\frac{\partial P}{\partial y}dtd\forall + + \int_t^{t+\Delta t}\int_{\forall}\nu\left(\frac{\partial^2 v}{\partial x^2}+\frac{\partial^2 v}{\partial y^2}\right)dtd\forall, \tag{11}$$

where $\int_{\forall} = \int_e^w \int_n^s$ and $d\forall$ correspond to $dxdy$.

This work, uses the (*Central Difference Scheme - CDS*), which can basically be obtained by an expansion of Taylor series, where terms involving second order or higher order derivatives are neglected, which guarantees a second order of spatial convergence - $O(\Delta x^2)$.

For the pressure-velocity coupling, the fractional step method was used, which basically segments the Navier-Stokes equation into two terms: predictor and corrector, as we can see in Nascimento (2016).

In order to estimate velocity fields, after some mathematical manipulations, the following equations were used:

$$\frac{u^* - u^t}{\Delta t} = \frac{P_e^t - P_w^t}{\Delta x} - \frac{F_e u_e^t - F_w u_w^t}{\Delta x} - \frac{F_s u_s^t - F_n u_n^t}{\Delta y} + \\ + \nu\left[\left(\frac{u_E - u_P}{\delta_{xe}} + \frac{u_P - u_W}{\delta_{xw}}\right)^t \frac{1}{\Delta x} + \left(\frac{u_P - u_N}{\delta_{yn}} - \frac{u_P - u_S}{\delta_{ys}}\right)^t \frac{1}{\Delta y}\right], \tag{12}$$

$$\frac{v^* - v^t}{\Delta t} = \frac{P_n^t - P_s^t}{\Delta y} - \frac{F_e v_e^t - F_w v_w^t}{\Delta y} - \frac{F_n v_n^t - F_s v_s^t}{\Delta x} + \\ + \nu\left[\left(\frac{v_E - v_P}{\delta_{xe}} + \frac{v_P - v_W}{\delta_{xw}}\right)^t \frac{1}{\Delta x} + \left(\frac{v_N - v_P}{\delta_{yn}} - \frac{v_P - v_S}{\delta_{ys}}\right)^t \frac{1}{\Delta y}\right], \tag{13}$$

where F are the fluxs on the elemental faces of the volume (e, w, n, s), velocities being evaluated using center difference schemes. Because we use offset mesh, the pressure is calculated exactly at the center of the main mesh as we can see on Fig. 3. Also in the same figure, we can see that: δ represents the distance between the centers of cells; Δ represents the length of the cell side; lowercase letters represents the value of some properties in the face of cell, where e, s, w and n is east, south, west and north respectively and the uppercase letters represent the cells, where E, S, W and N is east, south, west and north respectively. Finally, the pressure and velocity fields are corrected according to the fractional step method.

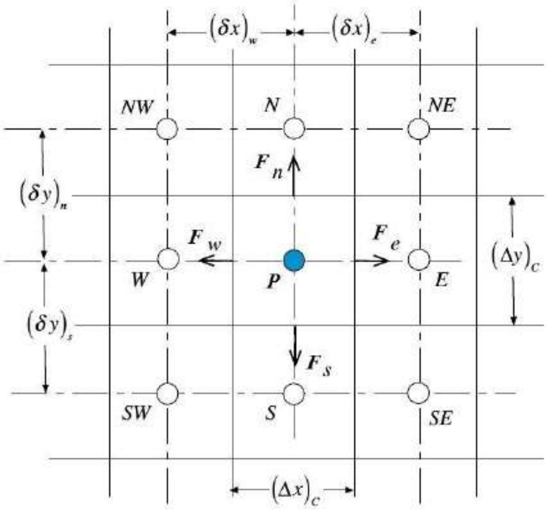

Figure 3: Geometrical entities used in the finite volume method, for a uniform two-dimensional mesh. Adapted from (Moukalled et al., 2015)

5 RESULTS

In this section, the results in which the cylinder is rotated will be displayed. This rotation is defined by the rate of rotation α, already discussed in section 3.1 . The vorticity fields, displacements and trajectories of the structure will be analyzed, as well as drag and lift coefficients, always with a parallel between reduced speed and rotation rate. For all cases studied, they were used: $\zeta = 0.0$ and $m^* = 2.0$. As already mentioned, the results in this section will use as reference the work of Zhao et al. (2014).

The rotation makes the vortex shedding flow asymmetric, which varies according to the direction of rotation adopted. The direction of counter-clockwise rotation was adopted, which explains the negative sign in some quantities that will be presented next in the next subsections.

5.1 Mean position of structure

The mean position is a simple way of verifying the influence of the rate of rotation on the behavior of the structure. As we can see in the Fig. 4, for $\alpha = 0$, in other words, no rotation, the cylinder displacement is symmetrical, which leads to the middle position of the cylinder around zero for all considered low speeds.

As the rate of rotation increases, we can see the appearance of an asymmetry in the oscillation of the cylinder, as shown by the variation of the average position of the cylinder. As mentioned, the average cylinder position tends to be negative because of the counter-clockwise rotation and tends to increase in modulus with the increase of the rotation rate.

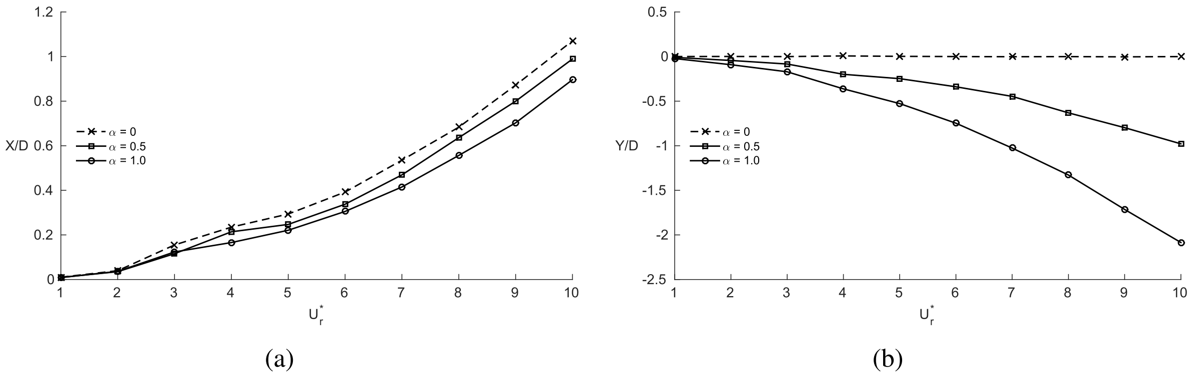

Figure 4: Mean position of the cylinder for the 2-dof VIV in the increasing U_r^* condition.

5.2 Trajectory of the structure

In this subsection, the trajectories developed by the cylinder are presented for several reduced speeds, analyzing the interference of α. As we can see in the Fig. 5(a), we have a cyclic and periodic behavior, in the shape of number 8, for the largest cylinder displacements. For $U_r^* \geq 6.0$, the trajectory begins to show random behavior with no defined pattern. If we compare with the results presented in the work of Zhao et al. (2014), under the same conditions, the trajectories presented by the structure should continue to present a well-defined pattern, but reducing in amplitude.

For the case with $\alpha = 0.5$, we have results that correspond well to those presented in the reference, but the largest displacement amplitudes occurred for smaller reduced velocities. When comparing with the work of Zhao et al. (2014), the largest displacements occur for $U_r^* = 5.0$, but in Fig. 5(b) we can see that the greatest displacement occurs for $U_r^* = 3.0$. For rotation rate, the pattern for low reduced speeds is circular, which changes to a more elongated and slender shape, reducing its amplitude as the reduced speed increases.

To analyze the case with $\alpha = 1.0$, it was divided into two graphs, Fig. 5(c) for reduced velocities less than five and Fig. 5(d) for speeds greater than five. For the cases with $U_r^* < 5,0$, the results are well identified with those presented in the literature, however they present the same question raised for $\alpha = 0$, so, there is an advance of the trajectories presented when analyzed in relation to the reduced speeds and the data presented in the reference. When we analyze the cases with $U_r^* > 5,0$, we can perceive total lack of pattern for the cylinder trajectories, results that do not match with Zhao et al. (2014).

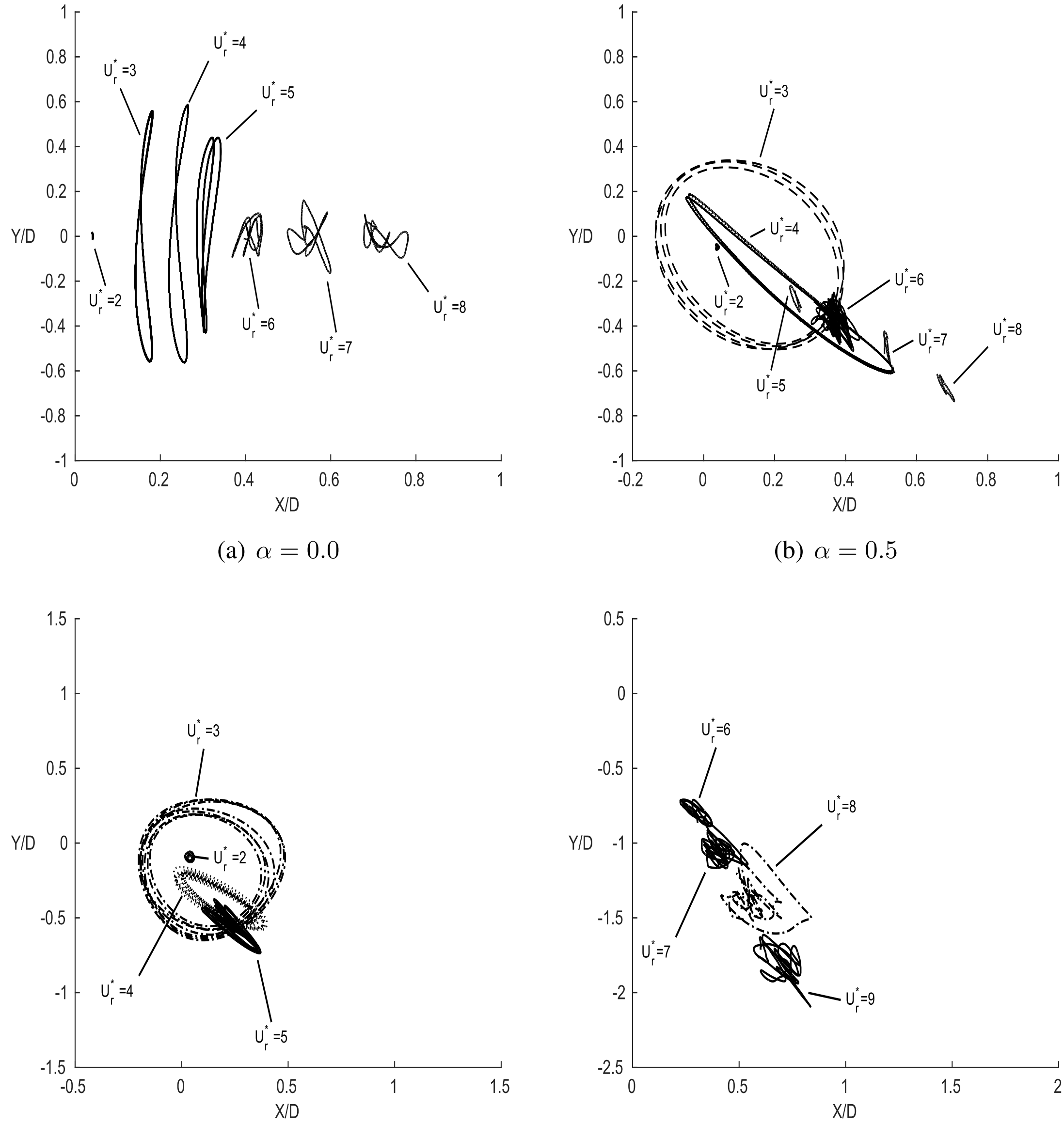

(a) $\alpha = 0.0$ (b) $\alpha = 0.5$

(c) $\alpha = 1.0$ (d) $\alpha = 1.0$

Figure 5: XY-trajectory of the cylinder under the increasing U_r^* condition for the 2-dof VIV.

5.3 Vorticity fields

The instantaneous vorticity fields of the flow were observed for several reduced velocities, varying the rates of rotation. To make the analysis more complete, the signs of the displacement in the directions x and y were added.

We can identify patterns in the flows and the respective changes that the increment in the reduced speed cause. From the case with $\alpha = 0$, seen in Fig. 6, we can identify the shape $2S$ in the vorticity fields shown in Figs. 6(b), (k) and (n). The $C2S$ pattern can be clearly identified in the vorticity field shown in Fig. 6(e). The case with $U_r^* = 4.0$ has standard $C2S$, but a little deformed, when compared to the case with $U_r^* = 3,0$. In the signs of displacements in the directions x and y, well-behaved signals are observed, with no presence of noise in both directions, reaching a steady state in a clear and defined way.

For the case with $\alpha = 0.5$, we are able to identify mixed patterns of structures and the signs of displacements in the directions x and y have distant modules, changing the patterns of the signals. Similarly to the commented for the case with $\alpha = 0$, we can identify the pattern $2S$ in Figs. 7(a), (j) and (m). For $U_r^* = 3.0$, there is a transition (region near the cylinder), which ends in the establishment of the pattern $C2S$, starting from a formation somewhat deformed to the said pattern away from the cylinder. On the other hand, with $U_r^* = 4.0$, it presents standard $2S$ tending to $C2S$. As we move away from the cylinder, we can identify the $C2S$ pattern.

Comparing the case with $\alpha = 0.5$ with the case without rotation, we can clearly see the influence of the rotation on the signs of displacements in the direction y. As the rotation induces an asymmetry in the mat and in the average position of the structure, as already mentioned in the previous sections, we can verify how it is responsible for changing the signals over time in both directions. Other information on these signals refers to the amplitude of displacement, which varies cyclically in the region of synchronization, later the signal shows much variation with amplitude and frequency.

The case with higher rotation rate, that is, $\alpha = 1.0$, of Fig. 8, shows greater interference of cylinder rotation. If we compare with the other cases, we can see how great the asymmetry of the treadmill downstream of the cylinder is. Similar to previous cases, it is still possible to identify patterns of structures, but greater interference and new modes. The $2S$ pattern appears clearly and deformed for the case with $U_r^* = 1.0$, as seen in the instantaneous vorticity field in Fig. 8(a). For $U_r^* = 8.0$ and $U_r^* = 10.0$, from Figs. 8(j) and (m), respectively, we observe a pattern that resembles $2S$, however asymmetric due to rotation and the new modes of oscillation that arise in the signs of displacements of directions x e y.

In a similar way, the identified and commented for $U_r^* = 3.0$, for the case with $U_r^* = 6.0$, Fig. 8(g), peculiarities in the pattern of structures formed in its treadmill are observed. At the beginning (region closest to the cylinder), a trend of formation of the $2S$ pattern can be identified. As it moves away from the cylinder, there is a pattern discontinuity and the treadmill looks smooth, returning to the standard $2S$. In an attempt to explain why the treadmill tends to be smooth, it can be seen that this occurs at the same time that the structure tends to change its behavior pattern, which as can be analyzed in the signs of displacements in the directions x and y occurs periodically over time, since it was not possible to obtain a homogeneous signal over time.

These peculiarities raised for the cases with rotation $\alpha = 0.5$ and $\alpha = 1.0$ can also be related to the contamination of the signals obtained by numerical noise, which contaminated the results presented in the previous sections and resulted in solutions which do not faithfully represent the physics of the problem.

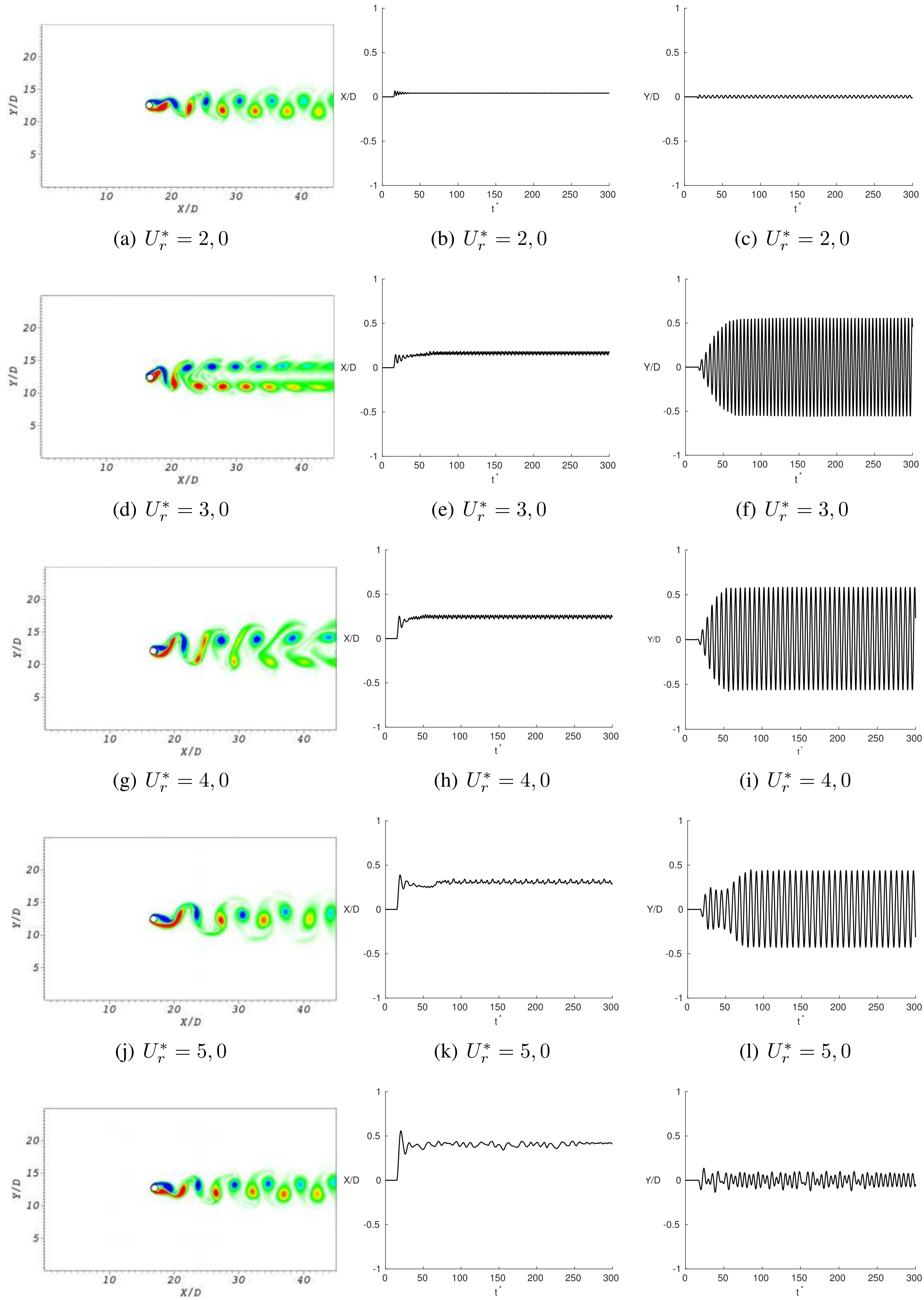

(a) $U_r^* = 2,0$ (b) $U_r^* = 2,0$ (c) $U_r^* = 2,0$

(d) $U_r^* = 3,0$ (e) $U_r^* = 3,0$ (f) $U_r^* = 3,0$

(g) $U_r^* = 4,0$ (h) $U_r^* = 4,0$ (i) $U_r^* = 4,0$

(j) $U_r^* = 5,0$ (k) $U_r^* = 5,0$ (l) $U_r^* = 5,0$

(m) $U_r^* = 6,0$ (n) $U_r^* = 6,0$ (o) $U_r^* = 6,0$

Figure 6: Instational fields of vorticities and displacements in the directions x and y, for cylinder with $2GL$ for several reduced speeds and $\alpha = 0$.

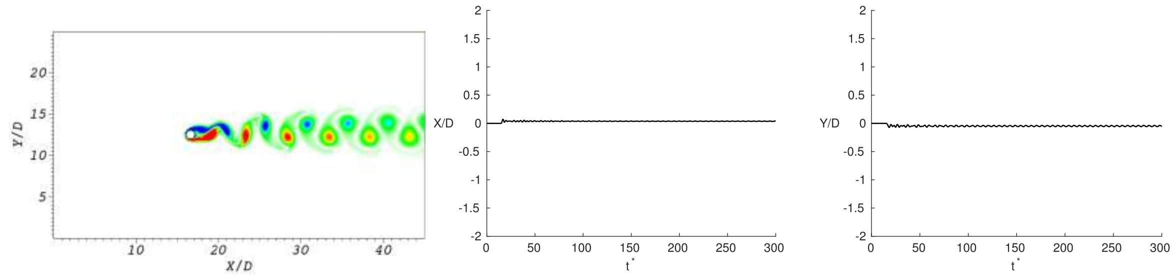

(a) $U_r^* = 2,0$ (b) $U_r^* = 2,0$ (c) $U_r^* = 2,0$

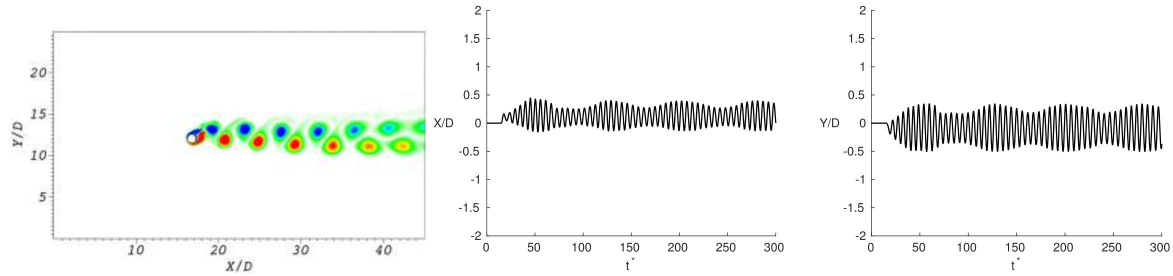

(d) $U_r^* = 3,0$ (e) $U_r^* = 3,0$ (f) $U_r^* = 3,0$

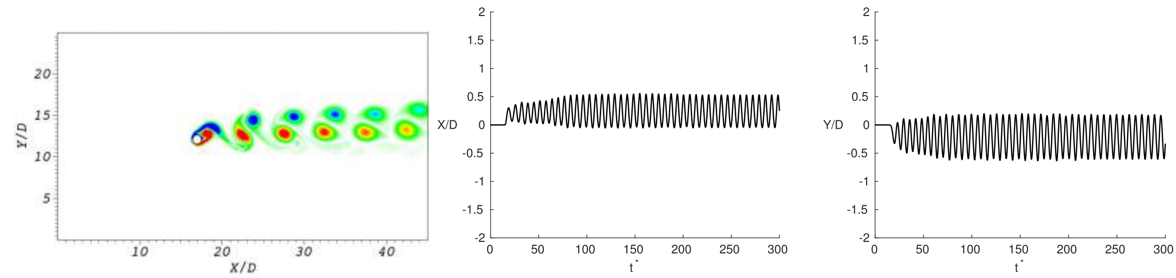

(g) $U_r^* = 4,0$ (h) $U_r^* = 4,0$ (i) $U_r^* = 4,0$

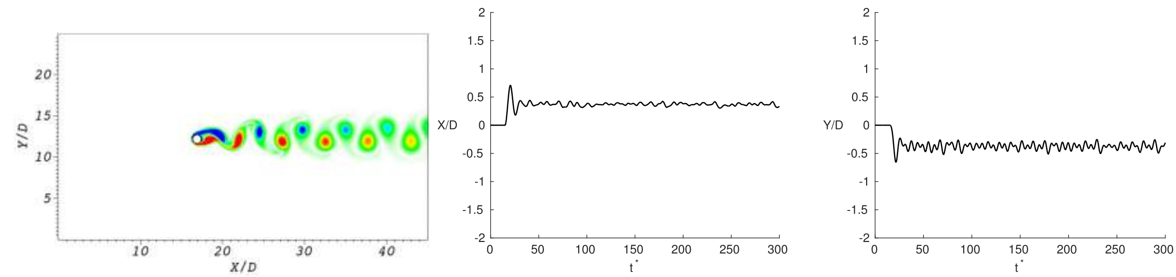

(j) $U_r^* = 6,0$ (k) $U_r^* = 6,0$ (l) $U_r^* = 6,0$

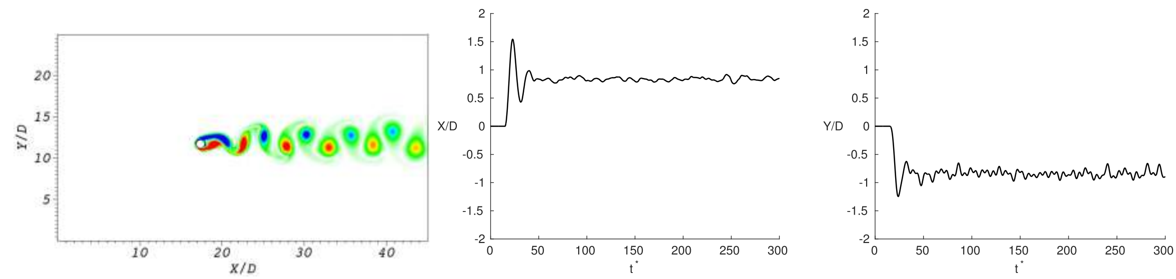

(m) $U_r^* = 9,0$ (n) $U_r^* = 9,0$ (o) $U_r^* = 9,0$

Figure 7: Instational fields of vorticities and displacements in the directions x and y, for cylinder with $2GL$ for several reduced speeds and $\alpha = 0,5$.

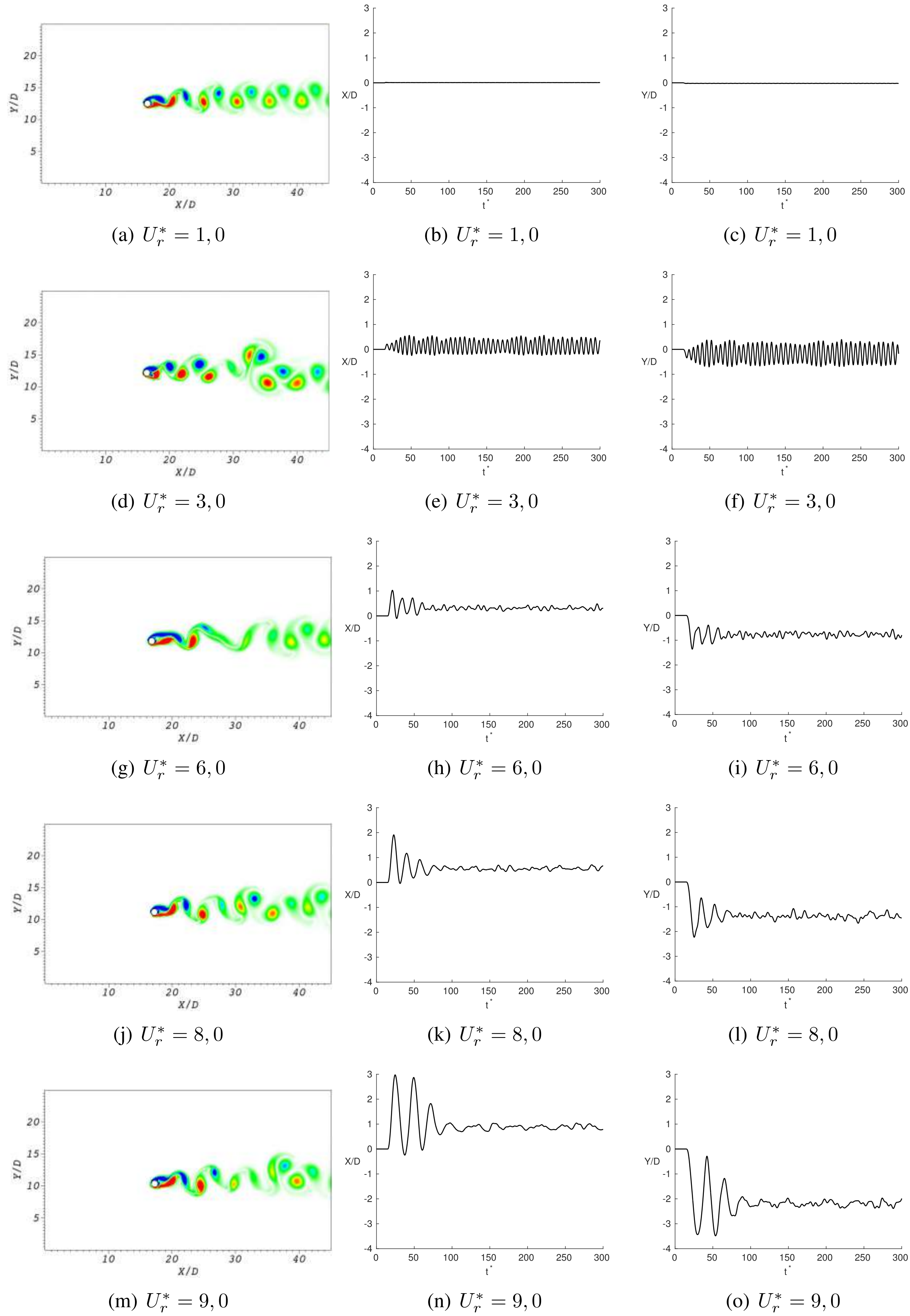

(a) $U_r^* = 1,0$ (b) $U_r^* = 1,0$ (c) $U_r^* = 1,0$

(d) $U_r^* = 3,0$ (e) $U_r^* = 3,0$ (f) $U_r^* = 3,0$

(g) $U_r^* = 6,0$ (h) $U_r^* = 6,0$ (i) $U_r^* = 6,0$

(j) $U_r^* = 8,0$ (k) $U_r^* = 8,0$ (l) $U_r^* = 8,0$

(m) $U_r^* = 9,0$ (n) $U_r^* = 9,0$ (o) $U_r^* = 9,0$

Figure 8: Instational fields of vorticities and displacements in the directions x and y, for cylinder with $2GL$ for several reduced speeds and $\alpha = 1,0$.

6 CONCLUSIONS

Vortex generation modes ($2S$ and $C2S$) could be observed for the different simulation conditions, well predicted in the literature, besides quantifying the influence of the rotation for given Re. We can observe good results when compared to the literature, but in some aspects, the observed numerical noise made it difficult to analyze the results and the consequent comparison between the cases, but the methodology was shown with potential to analyze this type of problem.

ACKNOWLEDGEMENTS

I thank the support agencies CAPES, CNPq and FAPEMIG that allowed this study to be carried out.

REFERENCES

Chern, M. J., Kuan, Y. H., Nugroho, G., Lu, T. and Horng, T. L., 2014. Directforcing immersed boundary modeling of vortex-induced vibration of a circular cylinder. *Journal of Wind Engineering and Industrial Aerodynamics*, pp. 109-121.

Moukalled, F., Mangani, L., Darqish, M., 2015. The Finite Volume Method in Computational Fluid Dynamics, vol. 113, Springer International Publishing, 2015, 791 pp.

Nascimento, A. A., 2016. Métodos pseudoespectral de Fourier e fronteira imersa aplicados a escoamentos presentes em engenharia dde perfuração. *PhD thesis, Federal University of Uberlândia*.

Su, S. W., Lai, M. C. and Lin, C. A., 2007. An immersed boundary technique for simulating complex flows with rigid boundary. *Computers and Fluids*, pp. 313-324.

Wang, Z., Fan, J. and Luo, K., 2008. Combined multi-direct forcing and immersed boundary method for simulating flows with moving particles. *International Journal of Multiphase Flow*, pp. 283-302.

Zhao, M., Cheng, L. and Lu, L., 2014. Vortex induced vibrations of a rotating circular cylinder at low Reynolds number. *Physisc of Fluids*, pp. 0-28.